PAPER

One-pot synthesis of photonic microparticles doped with light-emitting quantum dots†

Simone Bertucci, [ID] [a,b] Davide Piccinotti,[a] Mauro Garbarino,[a] Andrea Escher,[b] Gianluca Bravetti,[c] Christoph Weder, [ID] [c,d] Paola Lova,[b] Davide Comoretto, [ID] [b] Ullrich Steiner, [ID] [c,d] Francesco Di Stasio*[a] and Andrea Dodero [ID] *[b,c,d]

Colloidal quantum dots (QDs) exhibit size-dependent, tuneable optical properties that render them useful in a wide range of technological applications. However, integration of QDs into structured materials remains a significant challenge due to their susceptibility to degradation under chemical or physical perturbations. Here, we present a facile, scalable one-pot co-assembly strategy to embed commercially available CdSe/ZnS core–shell quantum dots into photonic microparticles *via* the confined self-assembly of a poly(styrene)-*b*-poly(2-vinylpyridine) block copolymer in emulsion droplets. The resulting hybrid particles exhibit a well-defined concentric lamellar structure and the quantum dots are selectively incorporated into the domains formed by the poly(2-vinylpyridine) blocks. This design enables two different optical responses, *i.e.*, vivid, non-iridescent structural colouration from photonic bandgap effects and stable engineered photoluminescence from the embedded QDs. The use of swelling agents provides an effective means to tune the photonic bandgap spectral position, extending the optical range to the entire visible region. Optical experiments reveal a subtle interplay between the photonic structure and QD emission, and the emission properties remain intact despite variations in the structural periodicity and matrix refractive index. This work highlights a robust platform for the integration of functional nanomaterials into photonic architectures, offering significant potential for applications in advanced light sources, displays, and sensing technologies. The simplicity of the approach, combined with its scalability, sets the stage for future exploration into hybrid photonic materials with tailored optical properties.

1. Introduction

Controlling and manipulating the interaction of light with materials is critical to advancing a wide range of modern technologies.[1] From optical communications to energy harvesting, photonic structures that consist of dielectric lattices in which at least two materials with different refractive indices are periodically alternated at the submicron scale have become indispensable.[2–4] These structures inhibit the propagation of light in specific spectral regions and directions,[5] a property that underpins their applications in fields as diverse as optical sensors, display technologies, solar cells, biomedical imaging,

[a]Photonic Nanomaterials, Istituto Italiano di Tecnologia, Via Morego 30, 16163 Genoa, Italy. E-mail: francesco.distasio@iit.it
[b]Department of Chemistry and Industrial Chemistry, University of Genoa, Via Dodecaneso 31, 16146 Genoa, Italy
[c]Adolphe Merkle Institute, University of Fribourg, Chemin des Verdiers 4, 1700 Fribourg, Switzerland. E-mail: andrea.dodero@unifr.ch
[d]National Center of Competence in Research Bio-Inspired Materials, Chemin des Verdiers 4, 1700 Fribourg, Switzerland
†Electronic supplementary information (ESI) available: Additional characterization data and fitting parameters. See DOI: https://doi.org/10.1039/d5nr00216h

and anti-counterfeiting.[6] Among the simplest yet most-studied structures, planar photonic crystals – also known as distributed Bragg reflectors (DBRs) – are optical structures consisting of alternating material layers with different refractive indices arranged periodically with sub-micron periodicity.[7] These structures inhibit the propagation of specific wavelengths of light, a process driven by coherent diffraction, which can be described in a simple way according to the Bragg–Snell condition.[8] The inhibited frequencies are known as photonic band gaps (PBGs) and can be easily tuned within the UV, visible and near-infrared spectral regions by controlling the periodicity and the refractive index of the alternating layers.[9] Such precise control makes DBRs attractive for various devices in applications such as mirrors, filters, waveguides, and resonators in optical communications and sensing technologies.[7]

Inorganic structures have shown outstanding performance due to the large dielectric contrast achievable among the building layers of DBRs,[10–12] but their fabrication is generally complicated. Producing such structures with polymers greatly benefits material availability, cost, and ease of fabrication.[13,14] Solution- or melt-based fabrication processes that apply to polymers – including spin/dip coating and co-extrusion – allow

for large-area structures at costs compatible with packaging technologies.[15] Polymer structures can redistribute the emission, enhance its intensity, and achieve low-threshold optically pumped lasing.[16,17] In addition, recent developments in all-polymer DBRs have enabled effects such as emission rate control and strong coupling,[18] offering significant potential for advanced optical applications.[19–24] However, planar DBRs are inherently limited by their angular dispersion, *i.e.*, the dependence of the PBG spectral response on the photon wave vector, which restricts their performance to a specific range of solid angles.[24]

One potential breakthrough is the fabrication of all-polymer photonic structures based on the self-assembly of block copolymers (BCPs) in confined environments.[25–27] BCPs consist of two or more immiscible polymer chains covalently linked. While the covalent bond prevents macrophase segregation, favourable interactions between identical blocks allow the spontaneous formation of well-defined nanostructures through microphase separation.[28] These nanostructures feature periodic domains with dimensions comparable to the wavelengths of visible light, making them well-suited for photonic applications when long-range order is achieved.[29] The self-assembly behaviour of BCPs is primarily governed by three factors: (i) the Flory–Huggins interaction parameter χ, which quantifies the interactions between different polymer blocks, (ii) the molecular mass of the block polymer, and (iii) the volume fractions of each polymer block. The size and morphology of the resulting nanostructures can be precisely controlled by tuning these parameters.[30–33] Confining the self-assembly of BCPs in emulsion droplets has recently emerged as a powerful strategy to fabricate photonic microparticles.[34–41] These exhibit a concentric or stacked lamellar structure, which gives rise to vivid, tuneable structural colours due to their ordered internal arrangement without spectral dispersion because of their spherical symmetry. Such microparticles retain the advantageous light-manipulating properties of planar photonic crystals but offer greater versatility in applications, particularly due to their ability to be used as liquid dispersions or in solid casting. However, the incorporation of nanoscale objects with emissive properties into photonic structures with high spatial precision is very challenging due to the sensitivity of these materials to external agents.[42] Interestingly, the co-assembly of BCPs and nanoparticles in emulsion droplets can lead to hybrid structures with precise spatial organization.[43,44] This can be achieved by exploiting ligands on the surface of nanoparticles that allow fine-tuning of their enthalpic or entropic interactions with the BCPs during self-assembly. Depending on the surface chemistry of these nanoparticles, they can be selectively incorporated into specific polymer domains, confined to the interfaces between them, or embedded in the core of the particles.[45,46] Despite these advantages, previous studies have only focused on low-molecular-weight BCPs and have not explored integrating light-emitting materials into self-assembled photonic microparticles. In particular, colloidal quantum dots (QDs) are attractive for this purpose due to their remarkable optical properties,

including high fluorescence quantum yield,[47] narrow emission linewidth,[48] and tuneable emission spectra based on particle size[49] and shape.[50] Their surface chemistry can also be easily modified, making them compatible with a variety of polymer matrices and solution-processing techniques.[47,51,52]

Here, we present a one-pot preparation strategy for hybrid photonic microparticles composed of poly(styrene)-*b*-poly(2-vinylpyridine) (PS-P2VP) and CdSe/ZnS core–shell QDs. Using a simple evaporation-induced confined co-assembly process in emulsion droplets, we achieved well-defined concentric lamellar structures and the selective incorporation of QDs into one of the BCP domains (*i.e.*, P2VP), as shown in Fig. 1. The fabrication starts with a biphasic mixture of chloroform, BCPs, and QDs in the dispersed phase and water and poly(vinyl alcohol) (PVA) in the continuous phase. The mixture was emulsified to form an oil-in-water (O/W) emulsion and as the chloroform slowly diffuses into the aqueous phase, the BCPs undergo spherical confinement within the droplets, which drives the self-assembly of the macromolecular chains into concentric lamellae. The resulting microparticles exhibit two different optical responses, *i.e.*, vivid, non-iridescent structural colouration and bright and stable photoluminescence (PL).

2. Experimental details

2.1. Materials

Poly(styrene)-*b*-poly(2-vinyl pyridine) (PS-P2VP, M_n = 213-*b*-215 kg mol^{-1} and M_w/M_n = 1.29) was purchased from Polymer Source. 3-Pentadecylphenol (PDP, purity ≥ 88%) was obtained from Santa Cruz Biotechnology. Blue, green, and red-emitting CdSe/ZnS core–shell (oleic acid-functionalized) quantum dots, chloroform (stabilized with amylene), homopolymer poly(styrene) (hPS, M_w = 35 kg mol^{-1}), poly(vinyl alcohol) (PVA, M_w = 13–23 kg mol^{-1}, 87–89% hydrolysed), and aluminium oxide (Al$_2$O$_3$, activated, basic, Brockmann I) were purchased from Sigma-Aldrich. The chloroform was treated with Al$_2$O$_3$ to remove stabilizers and degradation products before use. Milli-Q water with conductivity equal to 0.055 μS cm^{-1} was used for all the experiments unless otherwise indicated.

2.2. Methods

Photonic microparticle fabrication. PS-P2VP, PDP, and hPS were separately dissolved in chloroform to obtain solutions with a concentration of 10 mg mL^{-1}. Aliquots of the three solutions were mixed to obtain the desired ratio (x) between the pyridine groups and the PDP molecules. The final volume of all mixtures was kept constant at 0.25 mL. To this volume, 25 μL of quantum dot dispersion in toluene (5 mg mL^{-1}) was added and the resulting mixtures dried in a vacuum oven at T = 40 °C for a few hours to allow complete removal of the solvents. The resulting solid residue was redispersed in chloroform and used for the emulsification process. In a typical procedure, 0.25 mL of BCP-based solution in chloroform (with or without the QDs and the additives) were mixed with 2.5 mL of PVA aqueous solution (10 mg mL^{-1}) in a 7 mL glass vial and
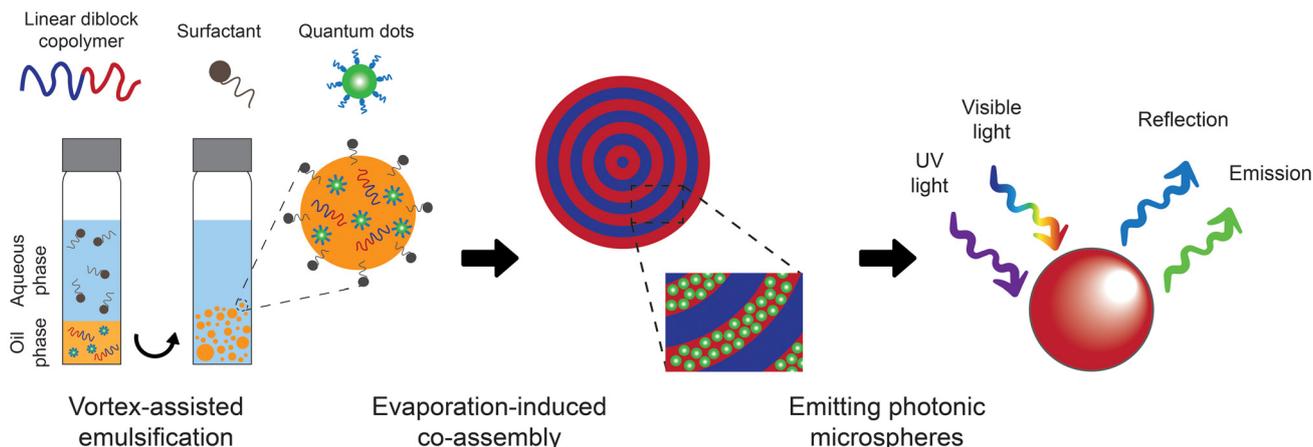
Fig. 1 Schematic of the process employed to produce the structurally coloured hybrid photonic microparticles incorporating light-emitting QDs. An oil phase (dispersed phase) containing both the block copolymer and the QDs was emulsified in an aqueous phase (continuous phase) and stabilized using poly(vinyl alcohol) (PVA) as a surfactant. The slow diffusion of the organic solvent through the aqueous phase allows the BCP chains to self-assemble into a well-defined concentric lamellar structure reflecting the blue region of the visible spectrum, while favourable ligand interactions on the surface of the QDs ensure their selective loading into only one of the block copolymer domains.

emulsified using a laboratory vortex mixer at 2500 rpm for 15 s. The as-prepared emulsions were poured into a glass Petri dish with a diameter of 5 cm containing 15 mL of PVA aqueous solution (3 mg mL^{-1}) and covered. The emulsion droplets were left to dry for 48 hours, after which the dried particles were collected, centrifuged at 5000 rpm for 30 minutes, and washed with 10 mL of Milli-Q water three times to remove excess surfactant. The solid deposit was finally dispersed in 2 mL of Milli-Q water.

Characterization techniques. Optical absorption measurements were performed using a Cary 300 spectrophotometer, whereas photoluminescence measurements were conducted using a Cary Eclipse spectrophotometer (excitation wavelength: 400 nm). Samples were prepared in quartz-glass cuvettes (light pass: 10 × 10 mm) by adding 30 μL of QD solution to 2.97 mL of toluene. For the blank, 3 mL of toluene was placed in a quartz-glass cuvette (light pass: 10 × 10 mm).

Transmission electron microscopy micrographs were acquired using a JEOL JEM-1011 instrument with accelerating voltage of 100 kV. Samples were prepared by drop-casting 10 μL of the diluted suspensions of QDs in toluene on the grids (Formvar/Carbon 200 mesh, Cu).

Optical microscopy of photonic microparticles was conducted using a custom-built microscope (ZEISS Axio Scope.A1) equipped with a diffusive CCD camera (Point Grey GS3-U3-28S5C-C) calibrated against a standard white diffuser and illuminated with a halogen lamp. Micrographs were captured in brightfield reflection mode configuration using a 50× objective (Zeiss LD EC Epiplan-Neofluar, NA = 0.8). Reflection spectra of the microparticles were acquired through micro-spectroscopy by coupling a microscope with a diode-array spectrometer (Ocean Optics QEPro) *via* an optical fibre positioned confocally to the microscope image plane (Avantes QP230-2-XSR, 230 μm core size) using an aluminium mirror as reference (Thorlabs

PF10-03-G01). The photonic microparticles were characterized on optical glass slides covered with a glass coverslip.

Focused-ion-beam scanning electron microscopy (FIB-SEM) (Thermo Scientific Scios 2 DualBeam FIB-SEM, FEI, Eindhoven, the Netherlands) was used to investigate the internal structure of the photonic microparticles. Particle suspensions were first drop-cast on aluminium stubs covered with conductive carbon tape and oven-dried at 40 °C under vacuum before being coated with a 4 nm thick gold layer. Half the microparticles were milled away using a Ga$^+$ ion beam set at an acceleration voltage of 30 kV and a current of up to 3 nA. The cut face was imaged using built-in SEM Everhart–Thornley (ETD, secondary electrons) and in-lens T1 (A + B composite mode, back-scattered electrons) detectors set to a voltage of 5 kV and a current of 0.4 nA. The image distortion induced by the acquisition at an angle of 52° was compensated with the built-in tilt correction feature. For each sample, the thicknesses of 20 lamellae of P2VP and 20 lamellae of PS were measured using ImageJ to obtain reliable statistical data. Confocal laser microscopy (CLM) was performed on single hybrid particles in suspension using a Leica LSM Stellaris 5 equipped with an HC PL Plan Apochromat 63×/1.40NA oil objective (brightfield, DIC). Three-dimensional images were reconstructed using Avizo software.

Ultra-small-angle X-ray scattering (USAXS) measurements were conducted on the ID02 beamline at the European Synchrotron Facility (ESRF) in Grenoble. Circular samples with an average thickness of 1 mm and a diameter of 4 mm were prepared by drop-casting particle suspensions in polytetrafluoroethylene (PTFE) disks closed on both sides using Kapton tape (DuPont).

Photoluminescence (PL) measurements were performed using a 405 nm diode laser at a repetition rate of 10 MHz and power of 13 nW through an optical microscope setup operated

in reflection mode with a 100× NA = 1.45 objective lens. The PL emission from the microparticles was collected through the same objective and measured using a single photon avalanche diode (SPAD) detector (Micro Photon Devices, PDM series) connected to a time-correlated single photon counter (TCSPC, PicoHarp300), allowing lifetime measurements. PL spectra were recorded using a Gemini interferometer (Nireos), which works in combination with the described SPAD detector and the TCSPC instrument to record the spectrum of the input light based on a Fourier transform approach. Samples were scanned using a piezo stage (PI, Physik Instrumente) capable of nanometer spatial resolution, resulting in a 2D map where a time trace (or lifetime) was recorded for each pixel. The value of each pixel was obtained by summing all the counts of the corresponding time traces. The time traces of the resulting 2D map were fitted with a double exponential function, which allows a time constant to be extracted from the fit for each pixel, resulting in a fluorescence lifetime image (FLIM).

3. Results and discussion

Colloidal QDs were selected as prototype materials to demonstrate the feasibility of fabricating emissive photonic microparticles via a one-pot process. We used commercially available blue- (bQDs, λ_{em}^{bQDs} = 470 nm), green- (gQDs, λ_{em}^{gQDs} = 530 nm), and red (rQDs, λ_{em}^{rQDs} = 650 nm)-emitting CdSe/ZnS core–shell QDs functionalized with oleic acid. Optical absorption, photoluminescence spectra, and transmission electron microscopy (TEM) micrographs of the QDs are shown in Fig. S1.† The absorption spectra (Fig. S1a–c,† black lines) of all three nanomaterials show a broad continuous background typical of colloidal QDs,[53] where distinct exciton peaks are detected at λ_{exc}^{bQDs} ∼ 465 nm, λ_{exc}^{gQDs} ∼ 520 nm, and λ_{exc}^{rQDs} ∼ 645 nm for the bQDs, gQDs, and rQDs, respectively. As expected, the intense fluorescence of the three samples (Fig. S1a–c,† coloured lines) is spectrally narrow with a slight Stokes shift (of about 5 nm) with peaks at 470 nm, 540 nm, and 650 nm for the different QDs. The TEM micrographs presented in Fig. S1a–c† show an almost spherical, homogeneous shape for all the QDs, whose average measured size increases from about 10 ± 1.2 nm for the blue QDs to 20 ± 2.0 nm for the red QDs. The correlation between the emission wavelength λ_{em} and the QD dimensions is related to quantum confinement effects.[54] In smaller QDs, the confinement of charge carriers in a limited volume increases their energy gap, leading to higher energy emissions. As the QD size increases, the energy gap decreases, resulting in lower energy emissions.[55]

QDs were then co-assembled with PS-P2VP in emulsion droplets without requiring specific, time-consuming surface modification. As mentioned, the co-assembly of BCPs and inorganic nanomaterials is challenging for several reasons. On the one hand, the QDs may prevent the BCP chains from self-assembly due to variations in enthalpy-driven interfacial interactions, structural strains, and entropy losses. On the other hand, the QDs themselves and their emissive properties are easily affected by changes in the external environment.[56] The nature of the organic ligand on the surface of the QDs plays a crucial role in this context, as it can establish interactions between the BCPs and the QDs and reduce the conformational entropic penalties on the BCP chains.[46] Additionally, specific interactions between the ligand and one of the blocks of the macromolecular chains can be exploited to facilitate control over the spatial distribution of the nanocrystals within the BCP structure. In this work, oleic acid-functionalized CdSe/ZnS quantum dots were selected on the expectation that the nitrogen atoms in the P2VP blocks would interact with the ZnS shell via electrostatic interactions, as previously reported in the literature.[57–59] Additionally, oleic acid provides solubility of the BCPs and the QDs in the same solvent (i.e., chloroform), thus allowing for the one-pot synthesis of the desired self-assembled concentric structures. To further confirm the dispersion of the oleic acid-capped QDs into the PV2P domains, the fabrication procedure described in Fig. 1 was carried out with PS-P2VP, as well as the poly(methyl methacrylate)-b-poly(2-vinylpyridine) (PMMA-P2VP) and poly(styrene)-b-poly(methyl methacrylate) (PS-PMMA) block copolymers. Fig. S2† shows that while the QDs are not embedded in the PS-PMMA microparticles (Fig. S2a–c†), they are homogeneously dispersed in one of the layers of the PS-P2VP or PMMA-PV2P microparticles (Fig. S2d–f and S2g–i†), thus confirming the affinity of the capped nanocrystals for the PV2P domains. Fig. 2a–d shows the reflectance spectra obtained using microspectrophotometry and the optical microscope images of the resulting PS-PV2P microparticles containing the different QDs (around 5 wt%). The reflectance spectrum of the QD-free microparticles obtained from the neat BCP shows a sharp reflectance peak at 420 nm (Fig. 2a), which corresponds to the bright, structural colouration visible in the centre of the particle in the optical microscopy image. Note that macroscopically, the microparticle dispersions do not present structural colour due to the low microparticle concentration and scattering effects. Upon co-assembly with the blue-emitting QDs, the reflectance peak is slightly redshifted to 425 nm. In addition, a second peak at 473 nm is detected and assigned to the bQD emission (Fig. 2b) caused by the white-light illumination of the sample. Similar observations are made for the microparticles containing gQDs and rQDs, for which the reflectance peaks are shifted to 443 nm and 471 nm, respectively. Again, additional peaks at 547 nm and 650 nm are observed and related to the emission of the green and red QDs, respectively. This spectral behaviour is reflected in the optical microscopy images, where all particles show a bright blue colour in the centre and a different coloured hue at the periphery, which is assigned to the emission of the QDs. Notably, the presence of QDs in the BCP structure slightly affects the spectral position of the PBG, which mainly indicates low impact on the self-assembly process and the final structure. The observed redshift can be explained by considering two factors. First, the embedded QDs have a much higher refractive index – above 2 – than the polymer layers (i.e., n_{P2VP} = 1.62 and n_{PS} = 1.59).[34,60,61] Consequently, selective loading of the QDs into the P2VP
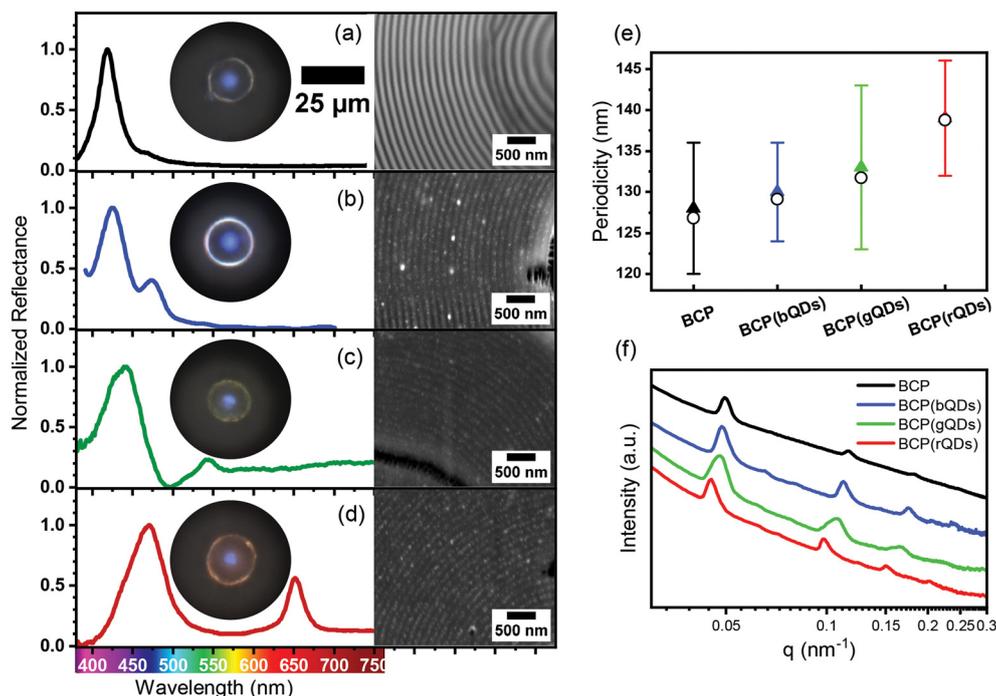
Fig. 2 (a–d) Normalized reflectance spectra of the individual, spherical microparticles. Data for particles consisting of the neat BCP (a) and the BCP containing blue- (b), green- (c), or red- (d) emitting QDs are shown. The circular insets show the optical microscopy images of the microparticles, while the right-hand images show the FIB-SEM micrographs of their cross-sections. (e) Lamellar periodicity measured from the FIB-SEM micrographs (triangles and error bars) and ultra-small angle X-ray scattering (USAXS) spectra (black empty circles). (f) USAXS spectra obtained with synchrotron radiation showing well-defined scattering peaks at progressively smaller q values due to the increase in structural periodicity.

domains is responsible for an increase in the dielectric contrast between the lamellar phases, resulting in a broader and redshifted photonic band gap compared to the bare structure, as described by the Bragg–Snell law adapted to the case of the photonic particles:[9]

$$\lambda_{\max} = 2D\sqrt{(d_{PS}\boldsymbol{n}_{PS}{}^2/D) + (d_{P2VP}\boldsymbol{n}_{P2VP}{}^2/D)}$$

with the periodicity structure D given by $d_{P2VP} + d_{PS}$. Second, the embedded QDs are responsible for a slight volume increase of the P2VP layers, further contributing to the shift in the photonic band gap to longer wavelengths. In particular, the larger size of the rQDs compared to that of the bQDs is expected to force the BCP chains to assume a more extended configuration, thus affecting the thickness of the lamellar structure. Detailed insights into the internal morphology of the particles are obtained by focused-ion-beam scanning electron microscopy (FIB-SEM), which is shown next to the respective spectra in Fig. 2a–d. Besides the fact that a concentric lamellar structure is clearly visible, verifying the selective and uniform dispersion of QDs consistently in only one of the two block copolymer domains (*i.e.*, P2VP layers, as discussed above) is possible. A similar uniformity in the spatial distribution of the QDs within the block copolymer particles is also verified by confocal laser scanning microscopy (CLSM) imaging (Fig. S3†). From the software-reconstructed three-dimensional images, homogeneous photoluminescence is

observed throughout the spherical volume for all three emitters, thus confirming the even spatial distribution of the QDs within the microparticles and the effectiveness of the proposed co-assembly procedure. Fig. 2e shows the domain periodicity D measured from the FIB-SEM micrographs. Although subject to considerable uncertainty, the trend is consistent with the gradual redshift of the PBG in the reflectance spectra (Fig. 2a–d) and indicates a progressive increase in the lamellar thickness due to the effect of the QD size on the self-assembly of the block copolymer chains. In particular, while no changes are observed in the PS layers (*i.e.*, $d_{PS} \sim 60$ nm), P2VP lamellae show a measurable increase in their size varying from $d_{P2VP}^{BCP(bQDs)} = 69.1 \pm 3.1$ nm to $d_{P2VP}^{BCP(rQDs)} = 78.8 \pm 5.7$ nm, further confirming that the QDs are localized in the P2VP domains. The same samples were analysed by ultra-small-angle X-ray scattering (USAXS) using synchrotron radiation.[62] The resulting scattering spectra are presented in Fig. 2f, while the periodicity data are shown in Fig. 2e as black empty circles. A distinct scattering peak (first order) is detected at $q = 0.0495$ nm^{-1} for the pure BCP particles, giving a periodicity of $D^{BCP} = 126.8$ nm. Similarly, values of $D^{BCP(bQDs)} = 129.1$ nm, $D^{BCP(gQDs)} = 131.7$ nm, and $D^{BCP(rQDs)} = 138.8$ nm were calculated for the samples loaded with different quantum dots. These results agree with the values measured from the FIB-SEM micrographs and, in particular, the well-defined scattering peaks indicate the ordered lamellar structure possessed by the particles and their homogeneity. Finally, by taking into

account the measured PBG spectral position (Fig. 2a–d) and the measured lamellar thickness (Fig. 2e), the Bragg–Snell law was used to qualitatively confirm the refractive index increase of the P2VP layers upon the addition of QDs. The measured spectral maximum for all hybrid samples, λ_{max}, is at higher wavelengths than the calculated values (Table S1†). However, given the limited spectral variations, this refractive index increase is considered minor and not particularly meaningful.

After investigating the optical response of the fabricated hybrid particles under white-light illumination, we further explored the emissive properties of the QDs embedded in the photonic microparticles. In particular, any potential changes in their optical properties due to the fabrication process of the hybrid structure and possible effects of the photonic structure were investigated.[63] Although the fabrication process is robust and reproducible, the microparticles exhibit some variability in their size distribution (*i.e.*, 20.7 ± 7.5 μm) and colour of the individual microparticles (Fig. S4†). Consequently, the detection of small changes in the photoluminescence of the QDs on a macroscopic scale becomes complicated and unreliable. For this reason, the emission of individual particles was measured using a microphotoluminescence setup and compared to the emission of the pure CdSe/ZnS QDs cast on a glass substrate. As previously highlighted, the spherical symmetry of the microparticles is responsible for the uniform colouration at their centre without any angle dependence (*i.e.*, the observed colour does not change with the observation angle).[34] In fact, the concentric multilayers can be approximated to be planar while aligning with the microparticle curvature so that they

could be locally considered as a planar dielectric mirror (when the measured spot size is much smaller than the particle diameter).

Steady-state photoluminescence (PL) spectra and time-resolved photoluminescence (TRPL) measurements are shown in Fig. 3. The photoluminescence spectra of the hybrid particles (Fig. 3a–c) present only minor variations in the spectral shape of the emission and a redshift of the emission wavelength is detected when comparing the PL of pure QDs to that of QDs embedded in the microparticles, with 14, 20, and 8 meV redshifts for blue-, green- and red-emitting quantum dots, respectively. While this effect can be attributed to the close packing of the QDs and possible self-absorption, the PL spectra show no sign of broadening. Furthermore, no spectral redistribution of the emission is detected due to the limited (*i.e.*, bQDs) or negligible (*i.e.*, gQDs and rQDs) spectral superposition of the emission peaks with the PBG of the microparticles, as shown in Fig. 2b–d. Additionally, the variable redshift observed for the bQDs, gQDs, and rQDs is most likely associated with the varying degrees of organic ligand coverage on the surface of the nanocrystals, which leads to a different tendency for aggregation during the self-assembly processes.

TRPL measurements (Fig. 3d–f) reveal faster decays for the QDs embedded in the photonic microparticles than in their neat form. The decay is well fitted in each case with a double exponential function, as reported in the ESI.† The average PL lifetime ($\bar{\tau}$), reported in each panel for all decays, shows 2.9-, 5.3-, and 1.7-fold decreases for the blue, green, and red-emitting QDs, respectively, when embedded within the block copo-
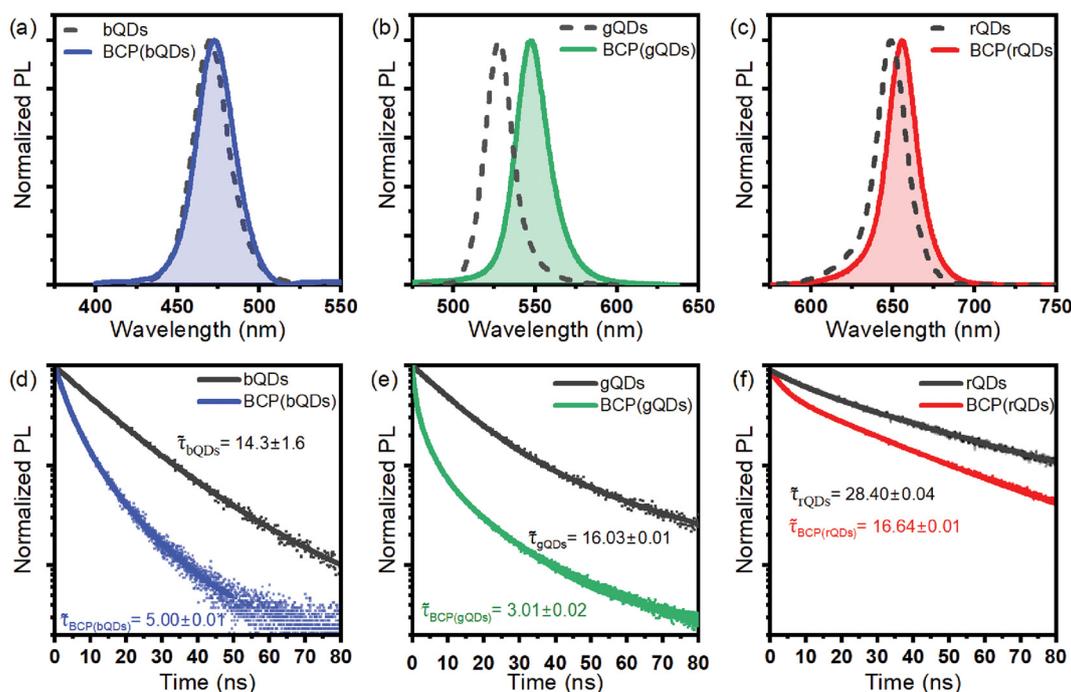

Fig. 3 Photoluminescence spectra of the (a) blue-, (b) green-, and (c) red-emitting QDs embedded within individual photonic microparticles (solid lines) and neat QDs (dotted lines). (d–f) Plots of fluorescence lifetime decay of the QDs embedded within individual photonic microparticles (coloured dots) and neat QDs (black dots).

lymer particles. The PL lifetime reduction of the quantum dots could be due to several factors. First, an environment with a higher refractive index than air can lead to faster radiative recombination processes.[64] Second, attractive interactions between oleic acid and P2VP may lead to the detachment of the ligands from the QD surface, resulting in the formation of defects that cause PL quenching, thus reducing the PL lifetime.[65] However, although evident, the variations in the decay time are considered only qualitatively as a quantitative evaluation would require a more in-depth and sophisticated characterization, which is beyond the scope of the present study.

To demonstrate the possibility of tuning the photonic structure of the microparticles containing the emitting QDs, a single type of emitter (*i.e.*, bQDs) was selected and the PBG of the microparticles was fine-tuned to ensure spectral overlap with the emission spectrum. To control the spectral position of the photonic bandgap, the periodicity of the lamellar struc-

ture was varied by adding swelling agents that increase the overall periodicity of the structure (*i.e.*, both lamellar layers are swelled simultaneously to ensure structural symmetry). Therefore, adding increasing amounts of additives to the BCP (bQD) precursor mixture allows for the controlled swelling of the lamellar structure and, thereby, a spectral redshift of the photonic bandgap. The additive of choice for swelling the P2VP layers is 3-pentadecylphenol (PDP), which has previously been demonstrated to interact selectively with the pyridine blocks *via* hydrogen bonding.[34,66] The samples thus made are classified according to the molar ratio (*x*-ratio) of PDP to pyridine residues. To maintain the balance between the volume ratio of the two blocks and to avoid a morphological transition away from the lamellar structure, counterbalancing amounts (the same volume as the added PDP) of a low-molecular-weight homopolymer poly(styrene) (hPS), which preferentially swells the PS domains, were added.[67] By varying the content of the
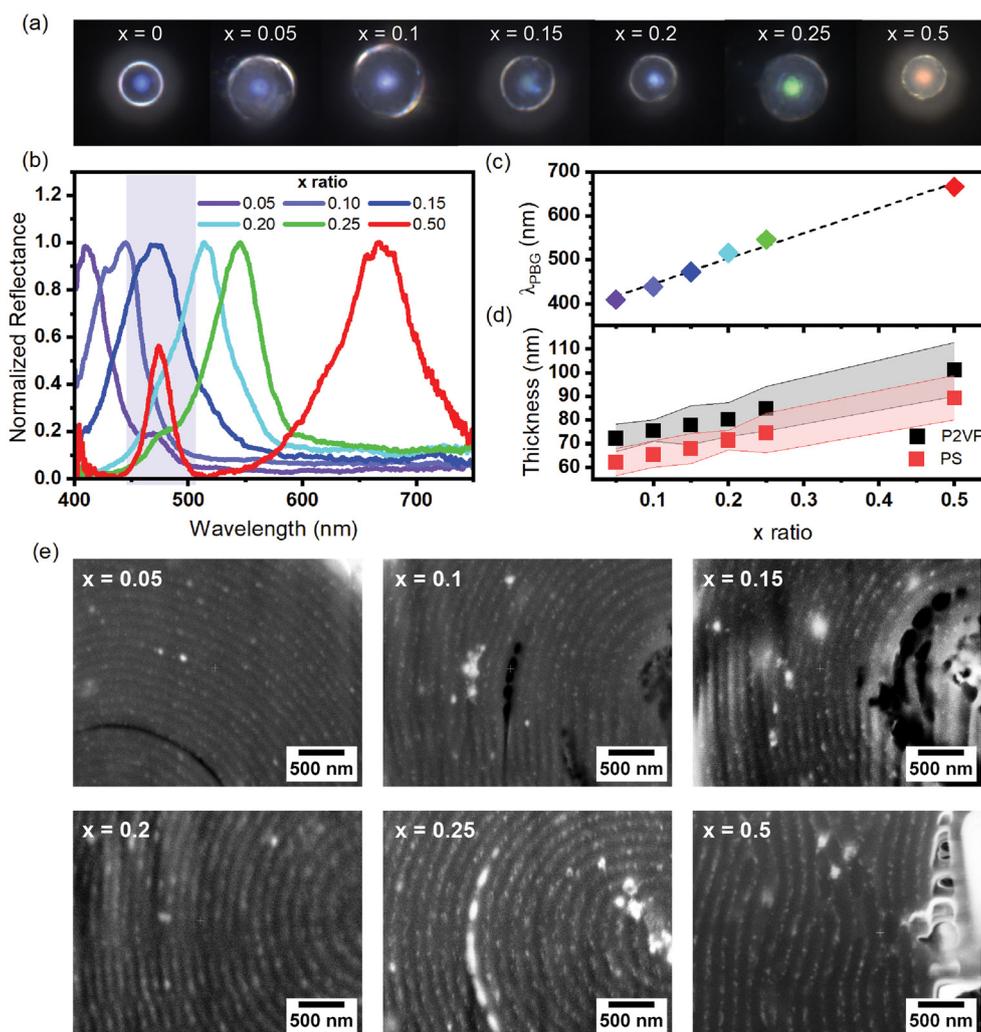

Fig. 4 (a) Optical microscopy images and (b) normalized reflectance spectra of the BCP(bQDs) samples containing increasing amounts of PDP and hPS additives. (c) Variation in the spectral position of the reflectance maxima as a function of the ratio of PDP to pyridines in the BCP (*x*). The black dashed line is a linear fit. (d) Thickness of the P2VP and PS lamellae as a function of the *x*-ratio of PDP to pyridines. (e) FIB-SEM cross-sections of the BCP(bQDs) particles for different *x*-ratios.

additives, the PBG can be tuned from λ_{max} = 410 nm (*i.e.*, x = 0.05) to λ_{max} = 666 nm (*i.e.*, x = 0.50), covering the entire visible spectrum, as shown in Fig. 4a–c. For all samples, the photoluminescence of the QDs is still clearly detectable at around λ_{em}^{bQDs} = 475 nm in addition to the bandgap signal, even under white-light illumination, suggesting that the emissive properties of the QDs are not affected by the swelling process.

It should be noted that adding a small amount of PDP (*i.e.*, x = 0.05) causes an initial blueshift of the PBG spectral position compared to the pristine block copolymer particles (Fig. 2b). This effect is attributed to the plasticizing behaviour of PDP, which allows the copolymer molecules to adopt different conformations.[68] However, increasing the amount of swelling agents induces a linear proportional redshift of the PBG (Fig. 4b) due to the increased layer thickness of the lamellar structure. The variation of lamellar thickness upon additive addition, measured from the FIB-SEM cross-sections, is shown in Fig. 4d, while the corresponding micrographs are shown in Fig. 4e for x-ratios of 0.05 (*i.e.*, lowest) and 0.50 (*i.e.*, highest). Similar to what was observed for the PBG, a nearly linear increase with increasing amounts of additives is observed for both the P2VP and PS layers. In all cases, the presence of QDs and their selective loading into P2VP domains is confirmed by the FIB-SEM micrographs, indicating that the additives do not alter the interactions between the QDs and the block copolymer chains. At the same time, the embedded QDs preserve the

possibility of fine-tuning the optical properties of the microparticles by adding small amounts of swelling agents.

After confirming the fine-tuning of the photonic bandgap, a systematic investigation of their emission properties was performed to elucidate any effects that arise from the photonic structure. Each sample was analysed using 2D photoluminescence intensity mapping of individual microparticles. First, an optical microscope equipped with a 100× oil objective was used to locate an isolated particle, where the emission intensity and lifetime were recorded over its surface area. Fig. 5a shows the photoluminescence map for the BCP(bQD) sample with an x-ratio of 0.15 (for other compositions, see Fig. S5a†) and the optical microscopy image of the particle is shown in Fig. 5b. The resulting map shows a uniform PL for most of the spherical microparticle surface, while lower intensities are observed at the edges where the amount of QDs is minimal, as shown in Fig. S6.† The fluorescence decay times (Fig. 5c) are consistent over the entire particle, indicating the uniformity of the effect on the exciton recombination process. Minor differences detected on the particle surfaces are assigned to a different dielectric environment of the exposed QDs. A comparison between the samples with different x-ratios (*i.e.*, different spectral positions of the PBG) was performed by analysing the PL intensity and lifetime signals acquired at the centre of the microparticles, where the structure has a geometry that can be approximated to that of a planar DBR. No significant variations are observed when ana-
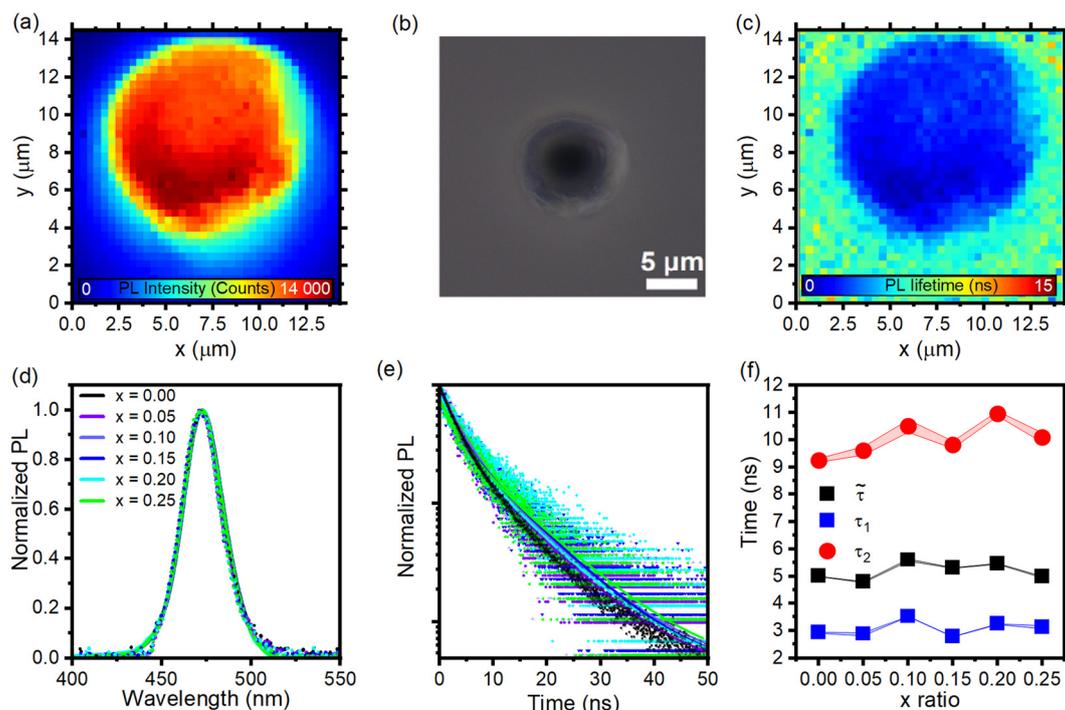

Fig. 5 (a) 2D photoluminescence map, (b) optical microscopy image, and (c) lifetime map showing the same emission behaviour throughout the photonic structure for a BCP(bQDs) microparticle with an x-ratio of 0.15. The complete dataset is shown in Fig. S5.† (d) PL spectra of individual BCP (bQDs) microparticles (solid lines) and water–dispersed microparticles (dotted lines) with different x-ratios. (e) Lifetime decays for individual water-dispersed microparticles with different additive contents. (f) Fitted emission lifetimes (τ_1 and τ_2) and their weighted average ($\tilde{\tau}$).

lysing possible differences in the shape and position of the photoluminescence (Fig. 5d, solid line). The emission is preserved when the microparticles are dispersed in water (Fig. 5d, dotted lines) and shows no difference compared to the single particles. This suggests that PDP does not significantly affect the oleic acid ligands on the quantum dot surface. If PDP interacts strongly with the ligands, we would expect aggregation phenomena, leading to a gradual redshift and broadening of the photoluminescence peak. Since no such effects are observed, we can conclude that PDP has minimal impact on the pristine ligand environment of the quantum dots. The lack of emission redistribution is attributed to the modest dielectric contrast (*i.e.*, $\Delta n \sim 0.03$ for PS *vs.* P2VP)[34] between the two materials comprising the photonic structure and the relative inhomogeneity of the layer thickness compared to the standard planar structures. These effects will likely limit the redistribution of the local density of photonic states and, thus, the field enhancement in the respective layers.[69] Therefore, it is realistic to consider that increasing the refractive index mismatch could lead to a more pronounced effect. Consistent with these data, the PL decay processes and their relative lifetimes remain unaffected by the addition of swelling agents (Fig. 5e). Indeed, Fig. 5f presents the two lifetimes of the particles (τ_1 and τ_2) and their weighted average ($\tilde{\tau}$),revealing that no significant differences are present.

4. Conclusions

In summary, we report a scalable one-pot co-assembly method for fabricating hybrid photonic microparticles that contain colloidal quantum dots. By leveraging the self-assembly of PS-P2VP block copolymers in emulsion droplets, we successfully produce particles with highly organized concentric lamellar architectures that exhibit vivid, non-iridescent structural colouration due to the refractive index mismatch between the ordered domains. Fine-tuning the thermodynamic interactions between the organic and inorganic components allows the selective incorporation of CdSe/ZnS QDs into the P2VP domains, effectively addressing integration challenges while preserving their photoluminescence properties. Additionally, we show that the incorporation of swelling agents offers a straightforward means to finely tune the photonic bandgap across the entire visible spectral range. This capability, achieved without compromising the QD emission properties, positions the fabricated hybrid particles as promising candidates for diverse applications in optoelectronics, sensing, and light-emitting devices. The robustness and simplicity of this fabrication process, combined with its adaptability to various nanomaterials and potentially other polymer systems, underscore its versatility for tailoring the optical properties of hybrid photonic materials. The demonstrated retention of QD emission under different structural configurations validates the method's efficacy, offering a reliable platform for the development of advanced photonic architectures with customizable functionalities. This innovative approach lays the groundwork for next-generation photonic devices, unlocking new opportunities in technology-driven applications.

Author contributions

SB contributed to the data curation, investigation, methodology and writing – original draft. DP contributed to the investigation. MG contributed to the investigation. AE contributed to the investigation. GB contributed to the investigation. CW contributed to the validation and writing – review & editing. PL contributed to the data curation and formal analysis. DC contributed to the supervision and validation. US contributed to the conceptualization, resources, validation and writing – review & editing. FDS contributed to the supervision, validation and writing – review & editing. AD contributed to the conceptualization, funding acquisition, methodology, project administration, supervision, validation, writing – original draft and writing – review & editing.

Data availability

Data for this article are available from Zenodo at **https://doi.org/10.5281/zenodo.14566782**.

Conflicts of interest

There are no conflicts to declare.

Acknowledgements

References

1 D. G. Baranov, M. Wersäll, J. Cuadra, T. J. Antosiewicz and T. Shegai, *ACS Photonics*, 2018, **5**, 24–42.
2 V. V. Vogler-Neuling, M. Saba, I. Gunkel, J. O. Zoppe, U. Steiner, B. D. Wilts and A. Dodero, *Adv. Funct. Mater.*, 2024, **34**, 2306528.

3   M. Bellingeri, A. Chiasera, I. Kriegel and F. Scotognella, *Opt. Mater.*, 2017, **72**, 403–421.

4   V. Berger, *Curr. Opin. Solid State Mater. Sci.*, 1999, **4**, 209–216.

5   J. B. Pendry, *J. Mod. Opt.*, 1994, **41**, 209–229.

6   M. A. Butt, S. N. Khonina and N. L. Kazanskiy, *Opt. Laser Technol.*, 2021, **142**, 107265.

7   E. Palo and K. S. Daskalakis, *Adv. Mater. Interfaces*, 2023, **10**, 2202206.

8   H. Chen, J. Wei, F. Pan, T. Yuan, Y. Fang and Q. Wang, *Adv. Mater. Technol.*, 2025, **10**, 2400865.

9   P. Lova, G. Manfredi and D. Comoretto, *Adv. Opt. Mater.*, 2018, **6**, 800730.

10 H. Kajii, M. Yoshinaga, T. Karaki, M. Morifuji and M. Kondow, *Org. Electron.*, 2021, **88**, 106011.

11 M. Portnoi, T. J. Macdonald, C. Sol, T. S. Robbins, T. Li, J. Schläfer, S. Guldin, I. P. Parkin and I. Papakonstantinou, *Nano Energy*, 2020, **70**, 104507.

12 J. Liu, D. Liu, Y. Shen, X. Yang, C. Zhao, R. Chen, Z. Yang, J. Liu, J. Ma and H. Xiao, *Opt. Mater.*, 2020, **107**, 110093.

13 G. C. Righini, J. Krzak, A. Lukowiak, G. Macrelli, S. Varas and M. Ferrari, *Opt. Mater.*, 2021, **115**, 111011.

14 Z. Wang, C. L. C. Chan, R. M. Parker and S. Vignolini, *Angew. Chem., Int. Ed.*, 2022, **61**, e202117275.

15 L. Peponi, D. Puglia, L. Torre, L. Valentini and J. M. Kenny, *Mater. Sci. Eng., R*, 2014, **85**, 1–46.

16 D. Huang, M. Zeng, L. Wang, L. Zhang and Z. Cheng, *RSC Adv.*, 2018, **8**, 34839–34847.

17 J. Xu, M. Hou, Y. Lu, L. Yang, J. Du, N. Li, H. Tan and L. Xu, *React. Funct. Polym.*, 2022, **173**, 105224.

18 A. Strang, V. Quirós-Cordero, P. Grégoire, S. Pla, F. Fernández-Lázaro, Á. Sastre-Santos, C. Silva-Acuña, P. N. Stavrinou and N. Stingelin, *Adv. Mater.*, 2024, **36**, 2212056.

19 H. Megahd, P. Lova, S. Sardar, C. D'Andrea, A. Lanfranchi, B. Koszarna, M. Patrini, D. T. Gryko and D. Comoretto, *ACS Omega*, 2022, 7, 15499–15506.

20 H. Megahd, M. Villarreal Brito, A. Lanfranchi, P. Stagnaro, P. Lova and D. Comoretto, *Mater. Chem. Front.*, 2022, **6**, 2413–2421.

21 M. Li, X. Lai, C. Li and Y. Song, *Mater. Today Nano*, 2019, **6**, 100039.

22 G. Canazza, F. Scotognella, G. Lanzani, S. De Silvestri, M. Zavelani-Rossi and D. Comoretto, *Laser Phys. Lett.*, 2014, **11**, 035804.

23 L.-T. Shi, F. Jin, M.-L. Zheng, X.-Z. Dong, W.-Q. Chen, Z.-S. Zhao and X.-M. Duan, *Phys. Chem. Chem. Phys.*, 2016, **18**, 5306–5315.

24 S. Wu, H. Xia, J. Xu, X. Sun and X. Liu, *Adv. Mater.*, 2018, **30**, 1803362.

25 J. J. Shin, E. J. Kim, K. H. Ku, Y. J. Lee, C. J. Hawker and B. J. Kim, *ACS Macro Lett.*, 2020, **9**, 306–317.

26 N. Yan, Y. Zhu and W. Jiang, *Chem. Commun.*, 2018, **54**, 13183–13195.

27 Y. Liu, F. Ke, Y. Li, Y. Shi, Z. Zhang and Y. Chen, *Nano Res.*, 2023, **16**, 564–582.

28 C. Cummins, R. Lundy, J. J. Walsh, V. Ponsinet, G. Fleury and M. A. Morris, *Nano Today*, 2020, **35**, 100936.

29 M. Stefik, S. Guldin, S. Vignolini, U. Wiesner and U. Steiner, *Chem. Soc. Rev.*, 2015, **44**, 5076–5091.

30 J. H. Kim, H. M. Jin, G. G. Yang, K. H. Han, T. Yun, J. Y. Shin, S. Jeong and S. O. Kim, *Adv. Funct. Mater.*, 2020, **30**, 1902049.

31 C. K. Wong, X. Qiang, A. H. E. Müller and A. H. Gröschel, *Prog. Polym. Sci.*, 2020, **102**, 101211.

32 T. J. Giammaria, F. Ferrarese Lupi, G. Seguini, K. Sparnacci, D. Antonioli, V. Gianotti, M. Laus and M. Perego, *ACS Appl. Mater. Interfaces*, 2017, **9**, 31215–31223.

33 G. Seguini, F. Zanenga, M. Laus and M. Perego, *Phys. Rev. Mater.*, 2018, **2**, 055605.

34 A. Dodero, K. Djeghdi, V. Bauernfeind, M. Airoldi, B. D. Wilts, C. Weder, U. Steiner and I. Gunkel, *Small*, 2023, **19**, 2205438.

35 U. Steiner and A. Dodero, *Chimia*, 2022, **76**, 826.

36 D.-P. Song, T. H. Zhao, G. Guidetti, S. Vignolini and R. M. Parker, *ACS Nano*, 2019, **13**, 1764–1771.

37 Z. Wang, C. L. C. Chan, T. H. Zhao, R. M. Parker and S. Vignolini, *Adv. Opt. Mater.*, 2021, **9**, 2100519.

38 Y. Yang, Y. Chen, Z. Hou, F. Li, M. Xu, Y. Liu, D. Tian, L. Zhang, J. Xu and J. Zhu, *ACS Nano*, 2020, **14**, 16057–16064.

39 Y. Yang, H. Kim, J. Xu, M. Hwang, D. Tian, K. Wang, L. Zhang, Y. Liao, H. Park, G. Yi, X. Xie and J. Zhu, *Adv. Mater.*, 2018, **30**, 1707344.

40 Q. He, K. H. Ku, H. Vijayamohanan, B. J. Kim and T. M. Swager, *J. Am. Chem. Soc.*, 2020, **142**, 10424–10430.

41 A. Escher, G. Bravetti, S. Bertucci, D. Comoretto, C. Weder, U. Steiner, P. Lova and A. Dodero, *ACS Macro Lett.*, 2024, 1338–1344.

42 B. Sarkar and P. Alexandridis, *Prog. Polym. Sci.*, 2015, **40**, 33–62.

43 T. N. Hoheisel, K. Hur and U. B. Wiesner, *Prog. Polym. Sci.*, 2015, **40**, 3–32.

44 Z. Deng and S. Liu, *Polymer*, 2020, **207**, 122914.

45 M. Xu, K. H. Ku, Y. J. Lee, J. J. Shin, E. J. Kim, S. G. Jang, H. Yun and B. J. Kim, *Chem. Mater.*, 2020, **32**, 7036–7043.

46 M. Xu, K. H. Ku, Y. J. Lee, T. Kim, J. J. Shin, E. J. Kim, S.-H. Choi, H. Yun and B. J. Kim, *Macromolecules*, 2021, **54**, 3084–3092.

47 P. Rastogi, F. Palazon, M. Prato, F. Di Stasio and R. Krahne, *ACS Appl. Mater. Interfaces*, 2018, **10**, 5665–5672.

48 O. Chen, J. Zhao, V. P. Chauhan, J. Cui, C. Wong, D. K. Harris, H. Wei, H.-S. Han, D. Fukumura, R. K. Jain and M. G. Bawendi, *Nat. Mater.*, 2013, **12**, 445–451.

49 J. Zhang, X. Zhang and J. Y. Zhang, *J. Phys. Chem. C*, 2009, **113**, 9512–9515.

50 X. Peng, L. Manna, W. Yang, J. Wickham, E. Scher, A. Kadavanich and A. P. Alivisatos, *Nature*, 2000, **404**, 59–61.

51 Y. Barak, I. Meir, A. Shapiro, Y. Jang and E. Lifshitz, *Adv. Mater.*, 2018, **30**, 1801442.

52 T. Pellegrino, L. Manna, S. Kudera, T. Liedl, D. Koktysh, A. L. Rogach, S. Keller, J. Rädler, G. Natile and W. J. Parak, *Nano Lett.*, 2004, **4**, 703–707.

53 A. P. Litvin, I. V. Martynenko, F. Purcell-Milton, A. V. Baranov, A. V. Fedorov and Y. K. Gun'ko, *J. Mater. Chem. A*, 2017, **5**, 13252–13275.

54 B. O. Dabbousi, J. Rodriguez-Viejo, F. V. Mikulec, J. R. Heine, H. Mattoussi, R. Ober, K. F. Jensen and M. G. Bawendi, *J. Phys. Chem. B*, 1997, **101**, 9463–9475.

55 A. R. C. Osypiw, S. Lee, S.-M. Jung, S. Leoni, P. M. Smowton, B. Hou, J. M. Kim and G. A. J. Amaratunga, *Mater. Adv.*, 2022, **3**, 6773–6790.

56 J. L. Casas Espínola and X. A. Hernández Contreras, *J. Mater. Sci.: Mater. Electron.*, 2017, **28**, 7132–7138.

57 M. Zhang, Y. Hu, Y. Hassan, H. Zhou, K. Moozeh, G. D. Scholes and M. A. Winnik, *Soft Matter*, 2013, **9**, 8887.

58 S. Singh, A. Horechyy, S. Yadav, P. Formanek, R. Hübner, R. K. Srivastava, S. Sapra, A. Fery and B. Nandan, *Macromolecules*, 2021, **54**, 1216–1223.

59 K. H. Ku, M. P. Kim, K. Paek, J. M. Shin, S. Chung, S. G. Jang, W. Chae, G. Yi and B. J. Kim, *Small*, 2013, **9**, 2667–2672.

60 A. Aubret, A. Pillonnet, J. Houel, C. Dujardin and F. Kulzer, *Nanoscale*, 2016, **8**, 2317–2325.

61 S. H. Mohamed and H. M. Ali, *J. Appl. Phys.*, 2011, **109**, 012108.

62 V. Bauernfeind, G. Bravetti, A. Dodero and V. V. Vogler-Neuling, *Bio-Inspired Photonic Structures for Optical Materials, European Synchrotron Radiation Facility (ESRF)*, DOI: **10.15151/ESRF-ES-1330737234**.

63 J. Kim, S. Song, Y.-H. Kim and S. K. Park, *Small Struct.*, 2021, **2**, 2000024.

64 M. Romero, J. R. Sánchez-Valencia, G. Lozano and H. Míguez, *Nanoscale*, 2023, **15**, 15279–15287.

65 C. Pu, X. Dai, Y. Shu, M. Zhu, Y. Deng, Y. Jin and X. Peng, *Nat. Commun.*, 2020, **11**, 937.

66 G. Moriceau, C. Kilchoer, K. Djeghdi, C. Weder, U. Steiner, B. D. Wilts and I. Gunkel, *Macromol. Rapid Commun.*, 2021, **42**, 2100522.

67 G. S. Doerk, R. Li, M. Fukuto and K. G. Yager, *Macromolecules*, 2020, **53**, 1098–1113.

68 T. Ruotsalainen, J. Turku, P. Hiekkataipale, U. Vainio, R. Serimaa, G. ten Brinke, A. Harlin, J. Ruokolainen and O. Ikkala, *Soft Matter*, 2007, **3**, 978.

69 H. Megahd, C. Oldani, S. Radice, A. Lanfranchi, M. Patrini, P. Lova and D. Comoretto, *Adv. Opt. Mater.*, 2021, **9**, 2002006.